

Research Article www.acsami.org

One-Step Large-Scale Nanotexturing of Nonplanar PTFE Surfaces to Induce Bactericidal and Anti-inflammatory Properties

Jian Xu, Haesoo Moon, Jinjia Xu, Jongcheon Lim, Thomas Fischer, Helen A. McNally, Herman O. Sintim, and Hyowon Lee*



Cite This: ACS Appl. Mater. Interfaces 2020, 12, 26893-26904



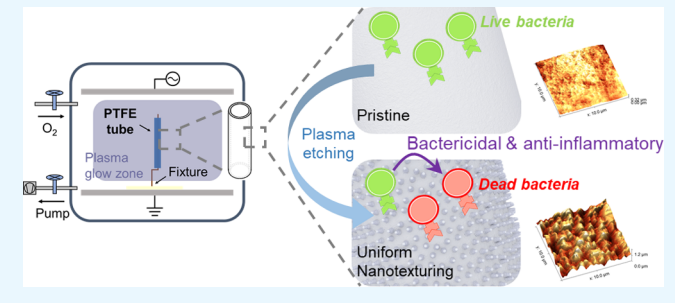
ACCESS

Metrics & More

Article Recommendations

s Supporting Information

ABSTRACT: Here we demonstrate a simple and scalable nanotexturing method for both planar (films) and nonplanar (tubes) polytetrafluoroethylene (PTFE) surfaces using a commercial desktop oxygen plasma etcher. The simple process can generate semiordered nanopillar structures on both tubular and planar samples with high radial and axial uniformity. We found that the resulting surfaces exhibit good in vitro bactericidal and in vivo anti-inflammatory properties. When tested against Staphylococcus aureus, the nanotextured surfaces showed significantly decreased live bacteria coverage and increased dead bacteria coverage, demonstrating significant bactericidal functionality. Moreover, the



etched planar PTFE films exhibited better healing and inflammatory responses in the subcutis of C57BL/6 mice over 7 and 21 days, evidenced by a thinner inflammatory band, lower collagen deposition, and decreased macrophage infiltration. Our results suggest the possibility of using this simple process to generate large scale biomimetic nanotextured surfaces with good antibiofouling properties to enhance the functionality of many implantable and other biomedical devices.

KEYWORDS: nonplanar etching, nanotexturing, plasma etching, bactericidal, anti-inflammatory surface, implantable material

■ INTRODUCTION

Implantable devices account for a quarter of all healthcarerelated infections in the United States, leading to a growing interest in materials with antifouling and bactericidal properties. These advanced materials can minimize incidences of implant revision, decrease the use of antibiotics, and increase the overall quality of medical care. Various approaches have been made to integrate novel bactericidal functionalities² including the usage of intrinsically³ or triggered⁴ antimicrobial materials, grafts loaded with antibiotics, mechanical actuation,⁶ nanoparticle loading,⁷ and nanotexturing.^{8–12} Among these approaches, biomimetic nanotexturing features several convenient advantages over other methods including wide applicability against a number of bacteria types, long shelf life, minimum postimplantation procedures, and minimum concerns over drug resistance development.

Found on the wings of cicada, 13 dragonflies, 14 and gecko skins, 15 naturally occurring nanostructures have previously been shown to have excellent bactericidal properties against both Gram-positive and negative bacteria. The bactericidal mechanism was recently postulated to be caused by the mechanical rupture of the bacterial membrane via both in vitro experiments and numerical modeling. 16,17 Further studies summarized that nanostructures with pillar-shaped morphology (approximately 50-250 nm in diameter, 80-250 nm in height, and 100-250 nm in spacing) have similar killing-upon-

contact mechanisms.⁸ Inspired by these recent studies, numerous materials, such as silicon, 18 metals, 19,20 and polymers, ²¹ with synthetic nanostructures have been fabricated using various techniques (e.g., nanoimprint, 22 hydrothermal synthesis, 23 laser treatment, 24 and metal-assisted chemical etching). 25

Several of these techniques demonstrate good scalability for mass manufacturing, including laser interference or colloidal photolithography to generate wafer-scale ordered nanoscale etch masks, ^{26,27} nanoimprinting to shape numerous preheated materials using a single negative mold, ²⁸ and plasma etching to generate high aspect ratio nanowires with ease.²⁹ However, most current nanoscale fabrication methods are designed for planar surfaces with the exception of nanoimprinted slightly curved surfaces for ocular applications.³⁰

These "mechano-bactericidal" nanotextures may be beneficial for implantable medical devices, as noted by great efforts to prevent biofilm development and infection on and near device surfaces. Many available in vitro and in vivo studies have already

Received: March 12, 2020 Accepted: May 21, 2020 Published: May 21, 2020





demonstrated that nanostructured surfaces have better biocompatibility, better ability to modulate cell behavior (e.g., adhesion, proliferation, and orientation), and better immune and inflammatory responses that lead to accelerated wound healing. However, *in vivo* studies on nanostructures with both bactericidal and anti-inflammatory properties are still scarce. With almost all implantable medical devices having nonplanar surfaces, there is a strong demand for a facile method for fabricating nanoscale features on large-scale nonplanar surfaces.

Plasma treatment can etch various polymer surfaces to form high aspect ratio nanoscale features.³⁵ Compared to other nanotexturing techniques, plasma etching requires no pre- or postfabrication processing, allowing for extremely simple, fast, low cost, and scalable manufacturing process. Moreover, plasma treatment is widely used already for removing contaminants, increasing hydrophobicity, depositing polymerized coating, improving adhesion, and enhancing implant integration.³⁶ Since plasma use is ubiquitous in medical device manufacturing for improved sterilization and biocompatibility, the potential utility of this plasma-induced nanotexturing is also quite high.

In this work, we demonstrate that this simple process can further be applied to nonplanar polytetrafluoroethylene (PTFE) surfaces to produce nanoscale pillar structures without any pretreatment steps. There are several studies that proposed mechanisms by which nanoscale structures can form on various polymer materials without masks using plasma etching. In general, there are two leading theories which include (1) nanotexturing due to redeposition of sputtered impurities³⁷ and (2) nanotexturing due to inherent surface morphology.³⁸ Here we demonstrate a maskless nanotexturing using simple oxygen plasma on both planar and nonplanar PTFE surfaces, which is widely used in implantable applications due to its high thermal, chemical, and dielectric stability (e.g., insulin cannula,³⁹ bioartificial liver,⁴⁰ maxillary sinus augmentation,⁴¹ and horizontal bone augmentation).⁴²

Using a commercially available radio frequency parallel-plate capacitively couple discharge plasma system and a bespoke fixture to vertically position nonplanar PTFE (tubes), we show that nanotexturing can be applied uniformly along the tube's radial and axial axes. We believe this is the first work to demonstrate the large-scale uniform nanotexturing on nonplanar implantable polymer surface. We evaluated these nanotextured surfaces for their bactericidal property against <code>Staphylococcus aureus</code> (S. aureus) and their resistance to physical abrasion by manual scratch and insertion into artificial and pork skin. Finally, we subcutaneously implanted the etched planar PTFE (films) into mice for 7 and 21 days to examine the anti-inflammatory effects of these nanotextured surfaces.

RESULTS AND DISCUSSION

Mechanism of Nanotexturing. Here we used a radio frequency parallel-plate capacitively coupled discharge plasma system to produce nanotextured surfaces. As shown in Figure 1a, oxygen (O_2) under low vacuum is subjected to an electromagnetic field with a radio frequency of 13.56 MHz, during which O_2 molecules are stripped of electrons and experience physical dissociation, resulting in a pool of charged or neutral particles with high-energy (i.e., plasma) contained between the upper power electrode and the lower ground electrode (plasma glow zone). When electrically insulated surfaces are exposed to plasma (e.g., PTFE films on the ground

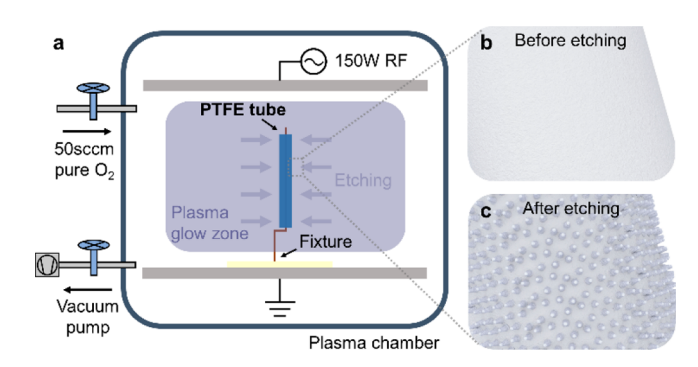


Figure 1. Schematic of the O_2 plasma etch system to create nanotexturing on nonplanar PTFE surfaces. (a) Nonplanar PTFE tubes are etched by vertically positioning them in the center of the plasma glow zone. (b,c) During the etching process, the outer surfaces of PTFE tubes are uniformly nanotextured with semiordered nanopillar structures.

electrode), a net negative bias is developed due to the higher mobility of electrons compared to positive ions, attracting high energy (typically $50-1000~{\rm eV})^{43}$ ion bombardment toward the surfaces, breaking C—F bonds (with dissociation energy of $5.6~{\rm eV})^{44}$ and etching the surface. We used this simple approach to create nanostructures on both planar PTFE films and nonplanar PTFE films. PTFE films were placed on the ground electrode of a plasma etcher (Figure S1) while the tubes were vertically positioned in the middle of the plasma glow zone (Figure 1a) to experience uniform plasma density and ion energy, as reported in both simulation and experiment studies. This resulted in a semiordered nanopillar structure with axial and radial uniformity (Figure 1).

As previously reported, polymer surfaces can develop semior well-ordered nanopillar structures via plasma etching. ^{29,35} While the definitive mechanism of such self-formation of nanostructures remains debatable, it is suggested to be due to the masking effects from redeposited impurities sputtered from the etching chamber³⁷ or due to inherent surface morphology (i.e., initial surface roughness). ³⁸ Morber et al. suggested that ion bombardment can strike the surface at different points of the native topology during plasma etching, which will lead to different interaction volume and varying local etch rates. ³⁸

We suspect that the inherent roughness is the main mechanism of nanostructure formation in our work for two reasons. First, masking impurities were typically reported in etchers with a higher plasma bias (e.g., reactive ion etching, RIE) or a higher plasma density (e.g., inductively coupled plasma, ICP), ⁴³ typically resulting in higher aspect ratio (>5) nanopillar structures. ⁴⁸ In the subsequent sections, we show that our nanostructures had a lower aspect ratio (<2) with no metallic impurities on the etched surfaces. Second, we show that the initial surface morphology differed for planar and nonplanar samples and the resulting nanotextures also differed in their pillar size, density, and spacing, which suggest that nanotexturing morphology may depend on initial roughness of the sample.

Nanotextured planar PTFE. Following the O_2 plasma treatment, we saw that the planar PTFE film surfaces were covered with semiordered nanopillar structures, as evidenced by the scanning electron microscopy (SEM) (Figure 2a-f) and the atomic force microscopy (AFM) (Figure 2g-i) images. Pristine PTFE films without etching showed microscale roughness with no observable nanostructure (Figure 2a,d,g).

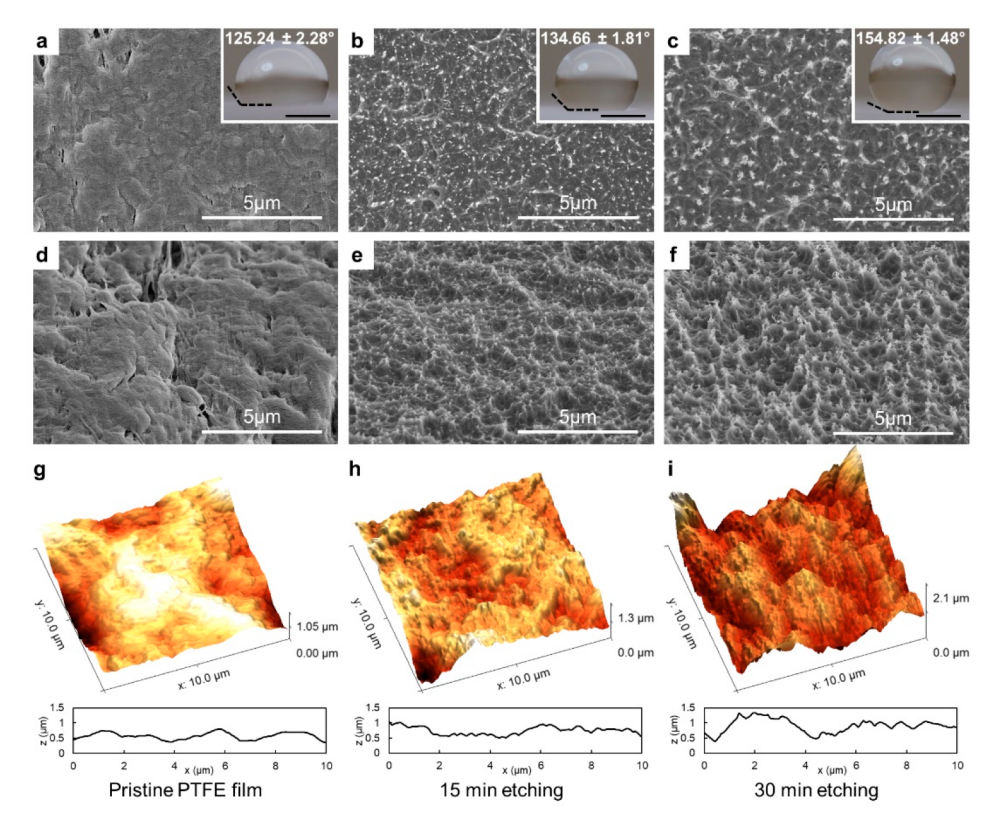


Figure 2. (a-c) Nontilted SEM, (d-f) 45° angled SEM, and (g-i) AFM results of pristine planar PTFE film and after 15 or 30 min of O_2 plasma etching. Insets in (a-c) show water droplets images (contact angles indicated by the dashed lines, scale bars = 1 mm). Plots in (g-i) show z-axis profile across the surfaces, captured by AFM.

Table 1. Measured Roughness (nm) and Surface Areas (μ m²) of Etched PTFE Surfaces (Scan Area = 100 μ m²)

	planar PTFE			nonplanar PTFE		
	mean roughness (R_a)	mean square roughness $(R_{ m q})$	total surface area	mean roughness (R_a)	mean square roughness $(R_{ m q})$	total surface area
pristine	102.90 ± 29.69	132.21 ± 37.41	107.42 ± 2.02	43.32 ± 14.19	55.15 ± 19.07	103.80 ± 1.82
15 min etching	128.70 ± 25.52	167.76 ± 34.71	126.84 ± 6.61	86.24 ± 10.18	108.70 ± 13.72	131.95 ± 17.72
30 min etching	207.74 ± 53.14	264.60 ± 68.26	141.82 ± 4.34	177.82 ± 23.82	220.05 ± 29.96	154.32 ± 15.48

The water droplet contact angle of the pristine PTFE film, which inherently has a low surface energy, 49 was 125.24 \pm 2.28° (Figure 2a inset, Figure S2). After 15 min of $\rm O_2$ plasma etching, we saw an increase in nanostructures compared to the pristine surfaces, indicated by the bright dotlike particles shown in SEM. These particles had a density of 1075.60 \pm 31.54 count/100 $\mu\rm m^2$ and the peak area (i.e., area of white dots) of 0.89 \pm 0.20 nm² (Figure 2b). Using 45° angled SEM and AFM, we confirmed the spikelike morphologies of these nanofeatures (Figure 2e,h) which had height of 264.63 \pm 60.05 nm. The water contact angle, after 15 min of etching, increased to 134.66 \pm 1.81° (Figure 2b inset, Figure S2). This increase in water contact angle may be due to the increased surface roughness as suggested by the Wenzel's model. 50

After 30 min of etching, we found that the bright dotlike particles became less dense (459.33 \pm 10.12 count/100 μ m²) but had larger peak area (1.52 \pm 0.47 nm²) (Figure 2c). The fabricated nanopillars had a height of 497.04 \pm 82.31 nm and spacing of 440.19 \pm 4.81 nm (Figure 2f,i). The water contact angle further increased to 154.82 \pm 1.48° (Figure 2c inset, Figure S2), making the surface superhydrophobic (>150°). This suggests that the water droplets on these samples are

suspended on top of nanoscale structures as described by the Cassie—Baxter model. 51

Using the AFM results, we calculated the roughness as well as the total surface area (versus scanned area) of the planar PTFE samples before and after the O₂ plasma etching (Table 1). A more detailed quantification of nanopillar structures is in Table S1 of Supporting Information. We found that the mean roughness (R_a) , the mean square roughness (R_a) , and the total surface area of all samples increased following etching, which suggests successful nanotexturing of PTFE surface using O2 plasma. Interestingly, we found that the height and peak area of nanopillars increased (from 264.63 \pm 60.05 nm and 0.89 \pm 0.20 nm² on 15 min etched films to 497.04 \pm 82.31 nm and $1.52 \pm 0.47 \text{ nm}^2$ on 30 min etched films) but decreased in density (from 1075.60 \pm 31.54 to 459.33 \pm 10.12 count/100 μ m²) with longer etching periods. We attributed this decrease in density to surface diffusion as described by the Bradley-Harper model, which suggested that nanoscale structures may be smoothed off during a prolonged plasma etching.³⁸ We also examined the planar PTFE films that were exposed to even longer etch times (45 and 60 min) and found that the resulting nanostructures feature a broader topography with increasing etch time (Figure S3).

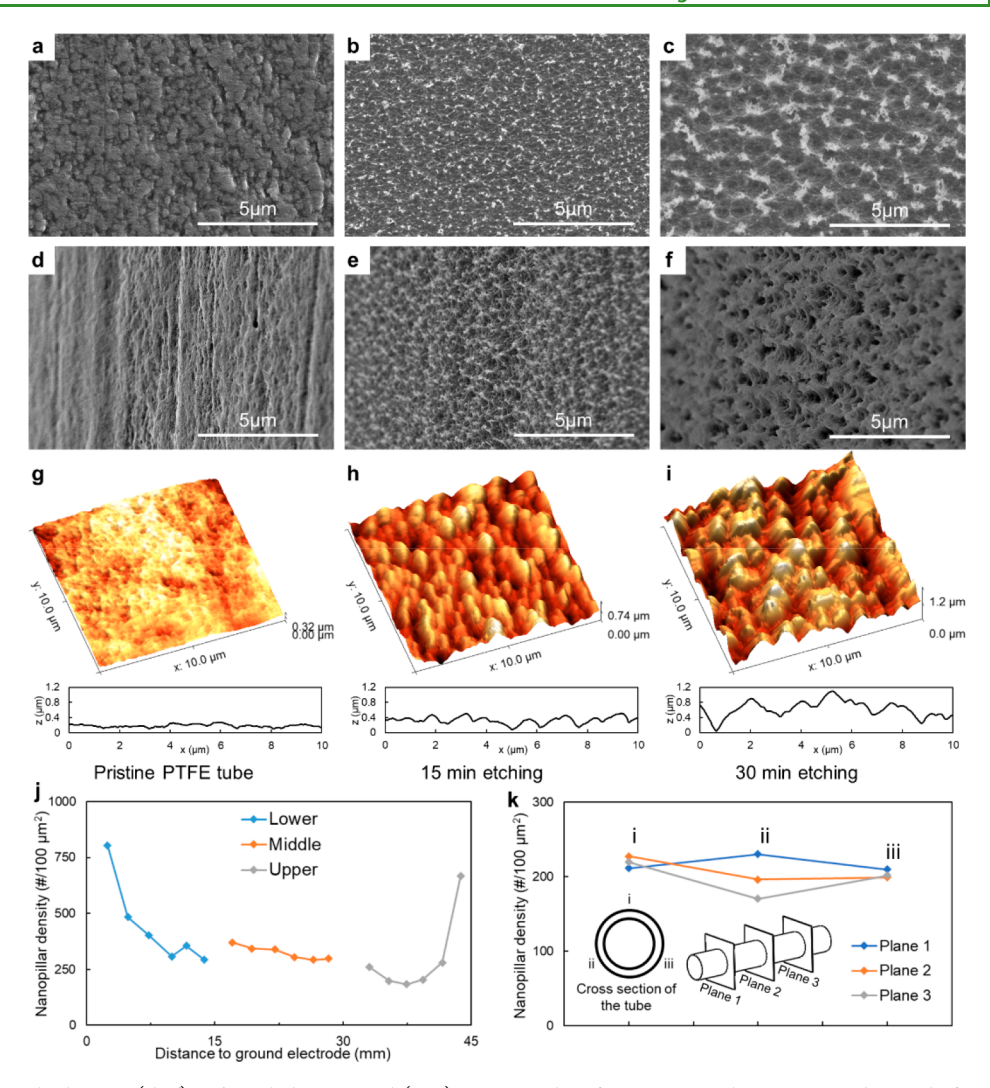


Figure 3. (a-c) Nontilted SEM, (d-f) 45° angled SEM, and (g-i) AFM results of pristine nonplanar PTFE tubes and after 15 or 30 min of O_2 plasma etching. Plots in (g-i) show the z-axis profile across surfaces. (j,k) Study of nanotexturing uniformity. (j) The nanopillar density of the 30 min etched PTFE tubes when they were positioned vertically in the lower, middle, and upper regions of the etching chamber, respectively. (k) On the same plane, 30 min etched PTFE tube surfaces had radially similar nanopillar density. Between different planes, etched PTFE tubes also had axially similar nanopillar density.

To verify that no traceable amounts of impurities were sputtered back onto the surface during etching, we examined energy-dispersive X-ray spectroscopy (EDS) result on the etched samples. We detected the presence of only carbon and fluorine before and after the O_2 plasma treatment (Figure S4 and Table S2), which suggests that masking from impurities may not be responsible for the nanotexturing observed here.

Nanotextured Nonplanar PTFE. After the O_2 plasma etching, we observed similar semiordered nanopillar structures on nonplanar PTFE tube surfaces (Figure 3). Like the planar PTFE films, the pristine PTFE tubes showed only microscale roughness (Figure 3a,d,g). After 15 min of O_2 plasma etching, PTFE tubes were covered with pillar-shaped nanostructures, confirmed by tilted SEM and AFM (Figure 3e,h). These nanopillars had a density of 405.16 ± 73.74 count/ $100 \ \mu m^2$, peak area of 3.44 ± 0.75 nm², and height of 265.05 ± 37.62 nm.

After 30 min of O_2 plasma etching (Figure 3c,f,i) the nanopillar structure became more pronounced. The nanopillar density decreased to 293.38 \pm 66.76 count/100 μ m², but the average peak area increased to 7.44 \pm 1.45 nm², and the height

increased to 578.20 \pm 61.93 nm. Also, $R_{\rm a}$, $R_{\rm q}$, and the total surface area of etched PTFE tube surfaces increased after the prolonged etching (Table 1). A more detailed morphology analysis of nanopillars on etched PTFE tubes can be found in Table S1. We believe the mechanism of nanostructure formation during O_2 plasma etching on nonplanar PTFE tube surfaces is similar to that of the planar PTFE film surfaces.

Our results suggest that the initial surface roughness may have played a key role in nanostructure formation. We saw in Figures 2a and 3a that the pristine PTFE surfaces appear to have distinct initial morphology in SEM. The AFM data confirm that planar and nonplanar PTFE samples had different initial roughness. Furthermore, both types of samples resulted in different surface roughness and nanostructure geometry following the plasma etching. For example, $R_{\rm a}$ increased from 102.90 ± 29.69 to 207.74 ± 53.14 nm (101.89% increase) after 30 min of etching for planar PTFE films, while it increased from 43.32 ± 14.19 to 177.82 ± 23.82 nm (310.48% increase) for nonplanar PTFE tubes. In addition, we observed more densely packed nanostructures in planar PTFE film than in nonplanar tube samples (Table S1). Since other factors (e.g.,

sample curvature, location) may also have significant effects, we will conduct additional experiments in the future to clarify the effects of intrinsic surface roughness on nanostructure formation. ^{52,53}

Uniformity of Nanostructure on Nonplanar PTFE. To ensure that nanotexturing can be uniformly applied on largescale nonplanar surfaces, we examined the location-dependent etching effects by varying the placement of PTFE tubes in the O2 plasma etching chamber. Nonplanar PTFE tubes were positioned in the plasma glow zone between the power and the ground electrodes in the etching chamber. As suggested by the Monte Carlo simulation and experimental studies of the radio frequency parallel plate capacitively coupled discharge plasma system, the middle region between the two electrodes has nearly the same levels of electron and ion densities. 45-Therefore, the electrically insulated PTFE tubes positioned in the middle region should theoretically experience nearly equal levels of ion bombardment induced by the negative bias at all surfaces, 43 resulting in uniform nanotexturing. To confirm this, we examined the axial and radial uniformity of 30 min etched PTFE tubes using SEM.

To study the axial uniformity of resultant nanostructures, three separate PTFE tubes were etched for 30 min at different positions: the lower, middle, and upper regions of the glow zone between the power and ground electrodes. The positioning of PTFE tubes was accomplished using a custom fixture that allowed them to be suspended with minimal contact (Figure 1a and Figure S5). The fixture had little effect on the formation of the nanostructures, as evidenced by similar nanostructure on samples placed directly on the ground electrode (Figure S6). We captured SEM images at different heights along the vertically positioned etched tubes (Figure S7) and counted the nanopillars to quantify their heightdependent densities (Figure 3). The PTFE tube positioned in the middle region had the greatest uniformity of nanopillar distribution. At the lowest measured point, nanopillars had a density of 370.36 count/100 μ m². At the highest measured point, nanopillars had a density of 298.42 count/100 μ m² (a decrease of 19%). However, for PTFE tubes positioned in the lower or upper regions of the glow zone, the differences were much bigger (64% decrease and 61% increase, respectively). The etched PTFE tubes had the highest nanopillar densities at places closest to the electrodes. This higher density of nanopillars may be due to an increase in plasma ion density. 45-47 Using these results, we determined that we can achieve good nanotexture uniformity in the middle region between the ground and power electrodes.

Figure 3k illustrates the radial uniformity at a single cross-sectional plane perpendicular to the vertical tube axis and parallel to the plasma electrode. To demonstrate the radial uniformity, we etched nonplanar PTFE tube surfaces for 30 min and quantified the nanostructure density on the three radially symmetrical faces (i, ii, and iii). We also measured along the length of the tube at three locations separated by \sim 4 mm (Planes 1, 2, and 3) and found similar nanostructure density all around the tube as well as along the length of the tube. SEM images taken at different locations along the tube surface all showed similar nanostructure morphology (Figure S7). Together, these results suggest that the O_2 plasma etching on nonplanar samples can produce a large scale nanotexturing with good axial and radial uniformity.

Resistance to Physical Abrasion. To withstand the clinical usage as implantable devices, the nanotextured surface

needs to have high resistance against physical handling and abrasion that can occur during a surgical procedure. To test, we intentionally abraded etched PTFE surfaces and examined the changes in nanostructures using SEM. For the etched PTFE films, we scratched them by hand (Figure 4a) or placed

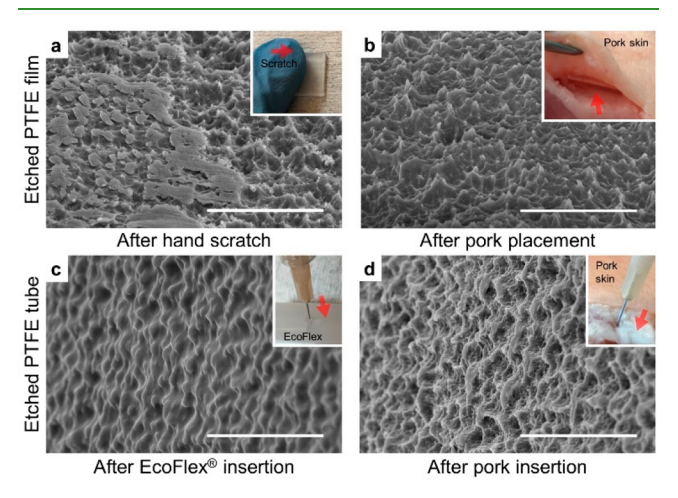


Figure 4. Resistance of etched nanotexturing against physical abrasion. PTFE films and tubes were etched for 30 min, then (a) scratched by hand, (b) placed into pork subcutis, (c) inserted into artificial skin (EcoFlex), or (d) inserted into pork subcutis and intramuscular space. After removal, samples were cleaned and examined using SEM. Insets illustrate the specific procedures performed. Scale bar = 5 μ m.

them into pork subcutaneous space (Figure 4b). For etched PTFE tubes, we inserted them into artificial skin (EcoFlex, Figure 4c) or pork subcutis and intramuscular space (Figure 4d). Planar nanostructures that underwent manual hand scratch were severely damaged and pillar tips were flattened as shown in Figure 4a. However, a considerable amount of nanopillars were intact, and nanostructures at the valleys between larger structures remained. We attributed this to the macroscale roughness of the etched PTFE films and high aspect ratio of the nanostructures which protect the entire surface from being flattened. PTFE films implanted in subcutaneous space maintained nearly all nanostructures upon insertion and removal (Figure 4b). PTFE tubes also maintained original etched morphology after artificial skin insertion (Figure 4c). However, the finer nanoscale roughness was smoothed out. Finally, PTFE tubes inserted into subcutis and intramuscular space maintained nanopillar structures, only experiencing slight bending of pillar tips (Figure 4d).

On the basis of these results, we concluded that the $\rm O_2$ plasma-etched nanostructures created on both PTFE films and tubes are somewhat resilient to physical abrasion but require careful handling. Although we observed some mechanical damages during certain procedures, most nanostructures remained unscathed. In practical application, we foresee nanotexturing to be applied only in areas that require minimal handling by surgical or implantation tools. As a part of our future work, we will better quantify the mechanical limitations of these nanostructures using a more systematic method, such as droplet impacting or pull tests. 34,49

Bactericidal Properties. Using a confocal microscope, we examined the coverage and survival of GFP-tagged *S. aureus* to evaluate the bactericidal properties of both planar and nonplanar PTFE surfaces. To contrast the live and the dead

bacteria, we used propidium iodide (PI) to stain damaged and punctured bacterial membranes. Figure 5 shows bacteria

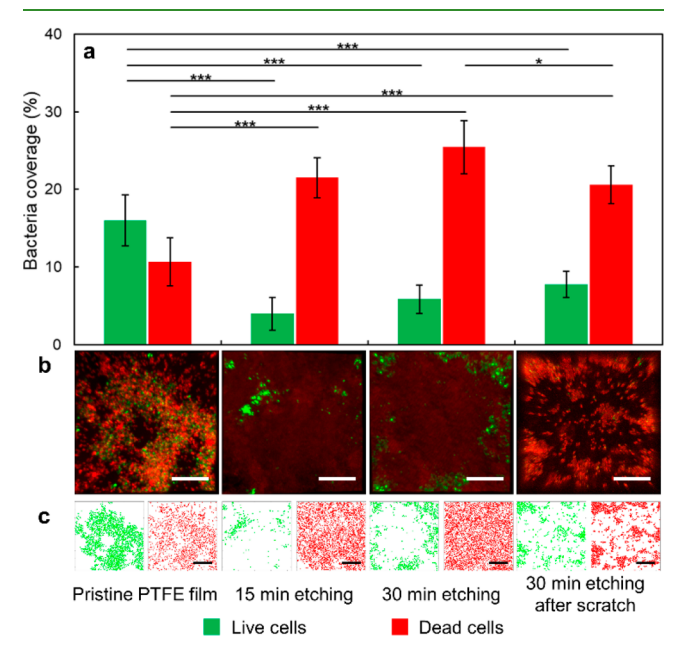


Figure 5. Bactericidal property of etched PTFE films against *S. aureus*. (a) Calculated bacteria coverage (%) of live *S. aureus* (green) and dead *S. aureus* (red) using (b) CLSM image and (c) rendered cell location and density. *, ***, and *** respectively indicate *p*-values lower than 0.05, 0.01, and 0.005 in one-way analysis of variance (ANOVA) with Bonferroni correction. Decreased live bacteria coverage and increased dead bacteria coverage on etched PTFE films suggest bactericidal property. Scale bars = $20~\mu m$.

coverage on pristine and etched planar PTFE films, and Figure 6 shows bacteria coverage on nonplanar PTFE samples. The quantified results in Table 2 show the change in bacteria coverage on etched PTFE surfaces compared to the pristine samples. Biofilms on pristine and etched PTFE surfaces were also fixed and examined using SEM (Figure S8). Both bacteria and surface morphologies of PTFE surfaces can be clearly observed. Etched PTFE surfaces (30 min) that underwent physical abrasion were also tested against bacterial adhesion and survival.

Our results showed significant decreases in live and increases in dead bacteria coverage on both planar and nonplanar nanotextured surfaces. For 30 min etched samples, the coverage of live bacteria decreased by 63.48% on planar PTFE films and 66.90% on nonplanar PTFE tubes. Conversely, the coverage of dead bacteria increased by 138.99% on planar PTFE films and by 83.34% on nonplanar PTFE tubes.

The PTFE films that underwent abrasion demonstrated less impressive bactericidal properties, indicated by a higher average live bacteria coverage and a lower dead bacteria coverage compared to the unabraded samples. However, the live bacteria coverage on scratched film was still significantly lower than that of pristine film, and the dead bacteria coverage on inserted tubes was significantly higher than pristine tube, which suggests that the abraded surfaces may still maintain some of its bactericidal properties.

When comparing the total bacteria coverage (live and dead) on etched PTFE surfaces with pristine ones, all cases had similar results without showing statistically significant difference (Table 2 and Figure S9). This indicates that *S. aureus*

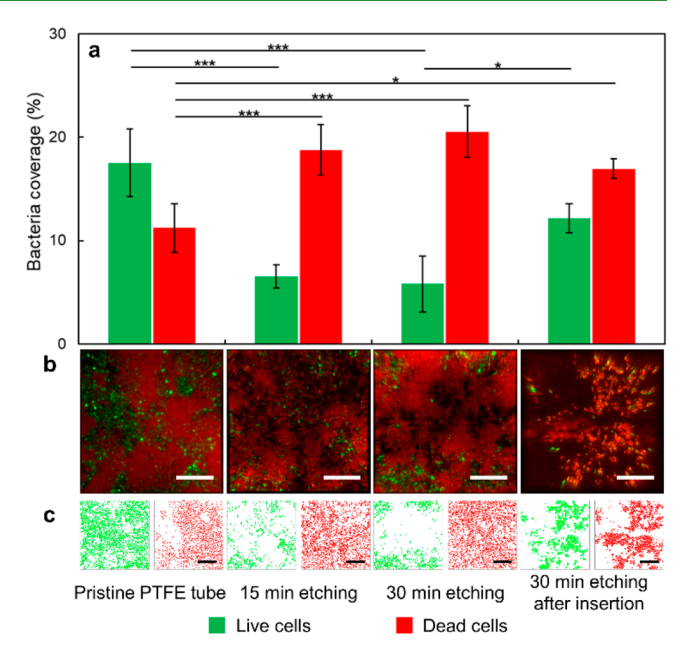


Figure 6. Bactericidal property of etched PTFE tubes against *S. aureus*. (a) Calculated bacteria coverage (%) of live *S. aureus* (green) and dead *S. aureus* (red) using (b) CLSM image and (c) rendered cell location and density. Decreased live bacteria coverage and increased dead bacteria coverage on etched PTFE tubes suggest bactericidal property. Scale bars = $20 \ \mu m$.

biofilms have nearly the same coverage on both pristine and etched PTFE surfaces and that bactericidal properties are enhanced by the addition of surface nanostructures, as opposed to bacteriostatic properties of pristine PTFE, which would otherwise prevent overall biofilm attachment and growth.

Previous studies have suggested that the bactericidal property of nanostructures originates from the interaction between the bacteria membrane and surface nanostructure. The deformation of bacteria membranes that is induced by gravity and van der Waals forces can cause excessive stretching across nanoscale morphologies which act as anchor points for cell adhesion. This excessive strain can lead to membrane rupture and cell lysis. To induce greater strain, it is reasonable to suspect that higher-density nanostructures of greater aspect ratio will improve the bactericidal properties. Here, planar PTFE films etched for 15 min demonstrated more dense nanostructures with better bactericidal property compared to 30 min etched surfaces. In the case of nonplanar PTFE tubes, surfaces etched for 30 min had better bactericidal properties potentially due to larger nanostructure heights.

The relationship between nanostructure (e.g., size, height, density, and aspect ratio) and bactericidal effects has recently been investigated using various models. The thermodynamic model proposed by Li et al. suggests that nanopillar surfaces with higher density and pillar radius have better bactericidal performance. Here, for both planar and nonplanar cases PTFE surfaces after 30 min of etching had an increase in dead S. aureus coverage. Consequently, we also observe that 30 min of etching results in a nearly doubled pillar radius with only a slight increase in pillar spacing, especially in nonplanar PTFE case. Though our experimental results align well with the trend proposed in the thermodynamic model, the effects of nanopillar heights and the curvature of the substrate still need to be investigated. Moreover, hydrophilicity or hydro-

Table 2. Change in S. aureus Coverage on Etched PTFE Surfaces to Compared to Pristine PTFE Ones

	PTFE films			PTFE tubes		
	live S. aureus	dead S. aureus	total	live S. aureus	dead S. aureus	total
15 min etching	-75.01%	+102.09%	-1.68%	-62.68%	+67.56%	-9.81%
30 min etching	-63.48%	+138.99%	+9.52%	-66.90%	+83.34%	-4.69%
after abrasion	-51.65%	+93.47%	+7.30%	-30.67%	+51.14%	+3.04%

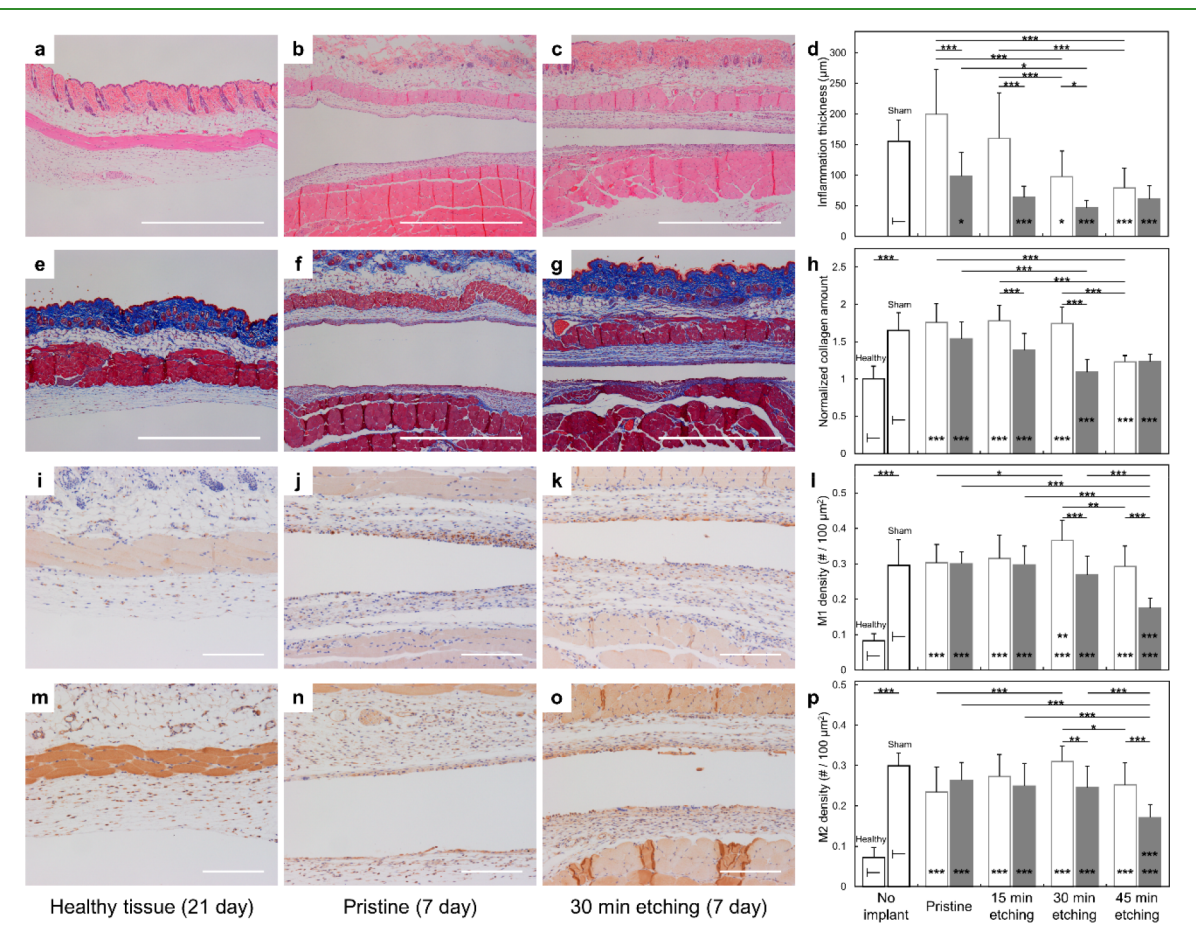


Figure 7. Histopathology results from *in vivo* study of subcutaneous implantation of PTFE films. Collected tissues were stained with (a-d) H&E, (e-h) MTC, (i-l) CD68, and (m-p) CD206. Tissues implanted with etched PTFE films (especially after 30 and 45 min etching) showed lowered inflammation band, collagen deposition, and M1 and M2 densities compared to pristine and sham groups, suggesting anti-inflammatory property of nanotexturing. Scale bars in (a-h) and (i-p) are 1 mm and 200 μ m, respectively. In quantification results, unfilled and filled bars represented samples collected at 7 and 21 days, respectively.

phobicity and pliability of pillars⁵⁷ may also play a large role in the functional effects of bacteria cell death. Tripathy et al. provided a thorough review of the various experimental and modeling approaches to link nanostructured materials with bactericidal effects.⁸

We conducted EDS to further verify that bactericidal effects were due solely to the formation of nanostructures induced by O₂ plasma etching. We examined the elemental composition of PTFE films etched for 15 and 30 min before and after etching. We also found prior work that suggests transient oxygen radicals may form on some O₂ plasma-etched surfaces.⁵⁸ Thus, we sought to examine the change in chemical composition over time (1–20 days) following the plasma treatment. By comparing the atomic ratio (Table S2) calculated using EDS spectrum (Figure S4), we observed no difference in carbon/fluorine ratio before and after etching or aging. Moreover, we found the amount of oxygen presented on the surface to be negligible as others have previously reported.^{59,60}

Foreign Body Response. To examine the biocompatibility and anti-inflammatory properties of O2 plasma-etched nanostructures, we subcutaneously implanted pristine and treated PTFE films (15, 30, and 45 min etching on both sides of the films) in mice for 7 or 21 days. Afterward, we explanted tissues surrounding the PTFE samples and compared against healthy tissue as well as tissue that underwent sham surgeries (explanted after 7 days). All animals healed properly with no indication of infection or observable inflammation. Histopathological analysis was conducted using hematoxylin and eosin (H&E) and Masson's trichome (MTC) stains. To quantify the effect of implant, we measured the thickness of the inflamed connective tissue and the total amount of collagen deposition surrounding the implant (Figure 7, panels a-d and e-h, respectively). We also quantified the density of classically activated macrophages (M1 macrophages) and alternatively activated macrophages (M2 macrophages) using CD68 and CD206 immunohistochemical stains (Figure 7i-p). A board-

Table 3. Qualitative and Quantitative Results of Tissues Collected from Subcutaneous Implantation Study of PTFE Films

group	grade	inflammation band thickness (μm)	normalized collagen amount	M1 density (#/100 μ m ²)	M2 density (#/100 μ m ²)
healthy	0		1.00 ± 0.17	0.08 ± 0.02	0.07 ± 0.02
sham	1	155.26 ± 35.12	1.65 ± 0.24	0.30 ± 0.07	0.30 ± 0.03
7 day pristine	0-1	199.86 ± 72.61	1.76 ± 0.25	0.30 ± 0.05	0.23 ± 0.06
7 day 15 min	1	160.33 ± 74.53	1.78 ± 0.21	0.31 ± 0.07	0.27 ± 0.05
7 day 30 min	1	97.80 ± 41.87	1.75 ± 0.22	0.37 ± 0.06	0.31 ± 0.04
7 day 45 min	1	79.44 ± 31.82	1.23 ± 0.09	0.29 ± 0.06	0.25 ± 0.05
21 day Pristine	1	98.71 ± 38.73	1.54 ± 0.22	0.30 ± 0.03	0.26 ± 0.04
21 day 15 min	1	64.18 ± 18.17	1.39 ± 0.22	0.30 ± 0.05	0.25 ± 0.06
21 day 30 min	1	46.55 ± 12.09	1.09 ± 0.17	0.27 ± 0.05	0.25 ± 0.05
21 day 45 min	0-1	61.08 ± 21.85	1.23 ± 0.10	0.17 ± 0.03	0.17 ± 0.03

certified veterinary pathologist also evaluated the quality of the surrounding connective tissue and the levels of macrophage infiltration in single-blind review (Table 3, criterion can be found in Table S3).

Figure 7a-c and Figure S10 show representative images of H&E staining. Figure 7d illustrates the comparison of the inflammation band. 61,62 In tissues that experienced sham surgery, we observed a layer of inflammation band with a thickness of 155.26 \pm 35.12 μ m. After 7 days, tissues implanted with pristine PTFE films had an increase in inflammation band thickness, reaching 199.86 \pm 72.61 μ m, which is expected due to the foreign body response. However, the observed inflammation band decreased for nanotextured samples, especially for films etched for 30 and 45 min. These samples had inflammation band thickness of 97.80 ± 41.87 and $79.44 \pm 31.82 \, \mu \text{m}$, respectively, showing significant decrease compare to the pristine films and even versus the sham group. After 21 days, inflammation band in all tissues experienced a 23.1-50.6% decrease in thickness, which is a sign of proper healing. Compared to the pristine samples, 15 and 30 min etched films still resulted in the thinnest inflammation bands after 21 days.

The representative images of MTC staining are shown in Figure 7e-g, followed by a comparison of the total amount of collagen deposition for each treatment group normalized to collagen deposits present in healthy tissue (Figure 7h and Table 3). The measurement protocol is adapted from work by Ibrahim et al. (additional images in Figure S11).62 Figure 7h shows that without any material implanted in the subcutaneous space, collagen deposition increased by 65% as a result of the surgical procedure to open a pocket in the subcutis. We observed similar amounts of collagen when pristine, 15 min etched, and 30 min etched PTFE samples were implanted over 7 days. However, PTFE films treated for 45 min induced collagen deposition at levels similar to the healthy tissue. Overall, the collagen amounts decreased between 7 and 21 days. The decrease in collagen is more clearly evident for films treated for 15 and 30 min, showing a 21.9% and 37.7% decrease, respectively. Compared to the pristine samples, 45 min etched PTFE samples resulted in a significantly reduced amount of total collagen.

Figure 7, panels i—k and m—o, shows representative images of tissues immunostained for CD68 and CD206 macrophagic markers, respectively (additional images in Figures S12 and S13). Using the color deconvolution function in ImageJ, we isolated blue macrophagic cells in the images. The number of cells was then counted and plotted as cell density in Figure 7l,p, respectively. Similar to the total collagen deposition, the density of both M1 and M2 macrophages present in the

connective tissue surrounding the implant pocket increased as a result of the surgical procedure to open the pocket. The M1 and M2 macrophages had similar densities when tissues were implanted with PTFE films (pristine or etched) with the exception of 45 min etched films experiencing a significant decrease in infiltration after 21 days. In addition, we saw increases in M1 and M2 macrophage densities for tissues implanted with 30 min etched PTFE films compared to the ones implanted with pristine films. While M1 and M2 macrophage infiltration did not change over 7 and 21 days when tissues were implanted with pristine and 15 min etched PTFE films, we saw significant decreases for 30 min (26.4% in M1 and 20.7% in M2) and 45 min (40.3% in M1 and 32.2% in M2) etched films. The ratio of M1/M2 macrophage densities also shows similar levels in all cases (Figure S14).

Lastly, the gradings of the collected tissue are presented in Table 3, which is given based on overall tissue conformity and composition, as well as neutrophil, macrophage, and foreign body giant cell infiltration. Results show that tissues in all groups only had minimal or mild acute inflammation (grade 1), demonstrating good biocompatibility of PTFE films and nanotexturing.

In general, thinner inflammation band, lower level of collagen deposition, and lower macrophage density are indicators of better implant integration. Thinner inflammation band and less collagen deposition with uniform and open structure are beneficial for metabolite exchange between the implanted materials and the host. 64,65 Here, both pristine and etched PTFE films facilitated a healthy layer of collagen fibroblasts in the surrounding connective tissue of the implant pocket. Tissues implanted with etched PTFE films showed thinner inflammation band and less collagen deposition, especially after 21 days of implantation and with 45 min etched ones. In some cases, the results are even better than the sham group and similar to healthy tissue, indicating the potential ability to accelerate healing. For macrophages, M1 type is generally considered to be pro-inflammatory while M2 type is presumed to be anti-inflammatory (or pro-healing), thus a lower M1/M2 ratio is a sign of anti-inflammation. In this work, all etched samples showed a lower M1/M2 ratio compared to tissues implanted with pristine PTFE films at 7 days (Figure S14). Although the decrease is marginal, tissue implanted with etched PTFE films had significantly lower densities for both M1 and M2 macrophages, which may suggest a better healing process. 63,66

CONCLUSION

In this study, we demonstrated a simple one-step maskless fabrication process to transfer nanostructures onto large-scale

planar and nonplanar PTFE surfaces. This process can generate axially and radially uniform nanostructures in scale by optimizing the material's etching position in a plasma chamber. The fabricated nanostructures are relatively resistant to minor physical abrasion during subcutaneous and intramuscular implantation, and they demonstrate significant bactericidal properties against S. aureus. Further, results from our in vivo study of PTFE films implantation in mouse subcutis revealed that the etched surfaces can mitigate the foreign body response and accelerate healing, quantified by thinner inflammation band, less collagen deposition, and fewer macrophage infiltration. Besides serving as implantable materials, nanotexturing on nonplanar surfaces has a wide range of other potential applications, including inducing hydrophobicity, 67,68 creating an antireflection surface, 69 and for energy harvesting.⁷⁰ Here, we show that our nanotextured PTFE may be useful as a surface functionalization method for implantable devices, which require passive bactericidal and anti-inflammatory properties. Nevertheless, additional evaluations are needed to confirm the bactericidal properties of such nanostructures against other types of bacteria (e.g., Gramnegative bacteria and antibiotic-resistant strains). Furthermore, the effects of fabrication parameters (e.g., etching gas, power, and time) on nanostructure (e.g., density, height, and aspect ratio) may be optimized. With additional data, it may be possible to use such a simple process to improve the lifetime of implantable devices that are often limited due to biofouling and the foreign body responses.

METHODS

Sample Preparation. Planar PTFE thin films with thickness of 50.8 \pm 7.6 μ m were prepared with virgin Teflon PTFE resins (McMaster Carr, Elmhurst, IL). The 12.7 × 12.7 mm pieces were cut and glued to diced microscope slides (Fisherbrand, Pittsburgh, PA) using silicone (Momentive, Waterford, NY) for ease of handling. Nonplanar PTFE tubes (inner diameter: 430 μ m, outer diameter: 700 μ m) were provided by Eli Lilly & Company (Indianapolis, IN) and cut into 15 mm pieces. All surfaces were thoroughly washed in 10% (v/v) micro-90 solution (Cole-Parmer, Vernon Hills, IL), rinsed with Milli-Q water (18.2 MΩ/cm, Burlington, MA), and dried at room temperature prior to etching and characterization.

Nanotexturing via O₂ Plasma Etching. A commercial desktop plasma etcher system (AP-300, Nordson March, Concord, CA) was used for processing the samples with 99.5% pure O₂ (Indiana Oxygen, Lafayette, IN) at a flow rate of 50 sccm. The planar PTFE films were etched by placing them on top of the ground electrode with power and the ground electrodes separated by 23 mm. The PTFE tubes were etched by positioning them vertically and in the middle between the power and the ground electrodes separated by 47 mm. Bespoke fixtures made of copper wire (28AWG, insulated with Polyurethane/ Nylon, Belden, St. Louis, MO) were used to batch process multiple tubes simultaneously. Etching was carried out at a chamber pressure of ~130 mTorr with etching power of 150 W and varying etching times. Such flow rate and etching power were selected to achieve the highest possible nanotexturing (Figure S15). Before each batch, the etching chamber was cleaned using 5 min of plasma exposure with the same conditions.

Surface Morphology Characterization. The 2D scanning electron microscopy (SEM) images of surfaces were captured using Hitachi S-4800 Field Emission SEM (Schaumburg, IL) with 5 kV as the accelerating voltage and analyzed using ImageJ. The 3D atomic force microscopy (AFM) images of surfaces were captured using Bruker BioScope Catalyst AFM (Santa Barbara, CA) in contact mode (nominal tip diameter: 20 nm, spring constant: 0.24 N/m) and analyzed using Gwyddion. Energy-dispersive X-ray spectroscopy (EDS) was carried out using Oxford X-Max^N 80 (Concord, MA)

working with Hitachi S-4800, during which surfaces of $12.5 \times 9 \mu m$ were scanned using electron beam with a 5 kV accelerating voltage and 15 μ A emission current, and X-ray signals were collected for 240 s. Before SEM and EDS, a thin layer of platinum (Pt) was sputtered using a desktop sputter coater (Cressington 208HR, Watford, U.K.).

Water Contact Angle (CA) Measurement. CA measurements were completed by analyzing the photographic pictures of water droplets on respective surfaces (pristine, 15 min, and 30 min etched PTFE films). Five microliter droplets were applied to the surfaces, and the CA of the static droplets were evaluated between the solid—liquid and liquid—air interfaces using MB-Ruler software. Measurements were taken in triplicate.

Physical Abrasion. PTFE films and tubes were etched for 30 min before testing for deformation caused by physical abrasion. Artificial skin was made using EcoFlex 00–30 (Smooth-On, Inc., Macungie, PA) with 1:1 Part A/B weight mixing ratio. Pork belly was used for subcutaneous and intramuscular implantation. Insertion of PTFE tubes was conducted with the help of a 30G needle threaded through the tubes' inner lumens. After insertion and removal, samples were sonicated in 10% (v/v) micro-90 solution and thoroughly rinsed with Milli-Q water before imaging.

Bactericidal Property Evaluation. Erythromycin-resistant Staphylococcus aureus (S. aureus) tagged with green fluorescent protein (GFP) were used to culture robust biofilms on PTFE surfaces. Prior to each experiment, bacteria subcultures were grown using 19:1:0.02 (v/v/v) tryptic soy broth (TSB, Becton Dickinson, Franklin Lakes, NJ):20% (w/v) glucose (Sigma-Aldrich, St. Louis, MO):erythromycin antibiotic at 37 °C for 12 h at 250 rpm. Growth cultures from day 1 were diluted 1/1000 in new growth medium. To facilitate bacterial attachment, PTFE surfaces were incubated in 5 mL 1:9 (v/v) poly-D-lysine (1.0 mg/mL, Sigma-Aldrich, St. Louis, MO):1X phosphate-buffered saline (PBS, Invitrogen, Carlsbad, CA) solution for 12 h at room temperature. Five milliliters of bacteria culture was aliquoted to each PTFE surface and incubated at 37 °C for 48 h at 50 rpm. After 48 h, 1.5 μ L of propidium iodide (PI, 20 mM in dimethyl sulfoxide) from LIVE/DEAD BacLight Bacterial Viability Kit (L7012, Invitrogen, Carlsbad, CA) was added into bacteria solution. After aspiration of bacteria solution and proper air drying, biofilms were imaged using a confocal laser scanning microscope (ZEISS LSM 880, Carl Zeiss, Jena, Germany)). Z-stack images at 100× magnification were taken and analyzed using Zeiss Zen software and MATLAB.

To acquire SEM images of bacterial biofilms, samples were fixed in 2.5% glutaraldehyde (Sigma-Aldrich, St. Louis, MO) in 0.1 M sodium cacodylate buffer (Sigma-Aldrich, St. Louis, MO) at 4 $^{\circ}$ C overnight, rinsed with 0.1 M sodium cacodylate buffer, postfixed in 1% osmium tetroxide (Sigma-Aldrich, St. Louis, MO) for 1 h, and rinsed in deionized water. Samples were then dehydrated in graded steps of ethanol (Sigma-Aldrich, St. Louis, MO)/hexamethyldisilazane (Sigma-Aldrich, St. Louis, MO) solution, air-dried, and Pt sputtercoated.

In Vivo Surgery. All animal experiments were previously approved by the Purdue Animal Care and Use Committee (PACUC). Thirty-three female six-week-old C57BL/6 mice (Taconic Biosciences, Rensselaer, NY) were randomly divided into 10 study groups. Each etching treatment of PTFE films (pristine, 15 min etch, 30 min etch, 45 min etch) was assigned to a short-term (7 days) implantation group and a long-term (21 days) implantation group (n = 3 per group). One group (n = 3) underwent sham surgery in which a pocket was opened but no material was implanted to provide a comparison of effects of surgery without any material implantation. Finally, one group (n = 6) did not undergo surgery; healthy tissue was collected from this group after 21 days.

PTFE films were prepared for implantation by cutting coupons from larger PTFE sheets which were pristine or previously etched on both sides. Coupons were cut using a Keyes cutaneous biopsy punch (Sklar Instruments, West Chester, PA) then sterilized by autoclave (20 min at 250 °F and 20 psi). Animals were acclimated for 4 days before preparing them for surgery. During subcutaneous implantation, animals were anesthetized and the dorsal interscapular region was

shaved and sterilized. A 1 cm incision and subcutaneous pocket was opened, and PTFE implants were inserted. After insertion, the surgical wound was sutured and animals were recovered from anesthesia. Twelve hours postsurgery, meloxicam (subcutaneous injection, 1–2 mg/kg) analgesic was administered. Animals were housed by Purdue Laboratory Animal Program (LAP) under standard conditions, including artificial day/night cycle, and water and rat pellet ad libitum. Pre- and postoperative care was conducted according to the established protocol. All animals survived surgeries without any complications. After 7 or 21 days of implantation, animals were sacrificed by anesthetic overdose, and PTFE implants and surrounding subcutis were explanted.

Tissue Processing. Tissues were fixed in 10% neutral buffered formalin between days 1–4. They were placed in a Sakura Tissue-Tek VIP6 tissue processor (Sakura Finetek, Torrance, CA) for dehydration through graded ethanols, clearing in xylene, and infiltration with Leica Paraplast Plus paraffin. After processing, tissues were embedded in Leica Paraplast Plus paraffin.

Microtomy. Tissue sections were taken at a thickness of 4 μ m using a Thermo HM355S microtome (ThermoFisher Scientific, Waltham, MA). Sections were mounted on charged slides and dried for 30–60 min in a 60 °C oven. After drying, all slides were deparaffinized through three changes of xylene and rehydrated through graded ethanols to water in a Leica Autostainer XL (Leica Biosystems, Wetzlar, Germany).

Histology. Using the Leica Autostainer XL, slides were stained in Gill's II hematoxylin, blued, and counterstained in an eosin/phloxine B mixture. Finally, slides were dehydrated, cleared in xylene and coverslipped in a toluene-based mounting media (Leica MM24). The Masson's trichome staining protocol was adapted from Carson et al.⁷¹

Immunohistochemistry. After deparaffinization, antigen retrieval was done with a TRIS/EDTA pH9 solution in a BioCare decloaking chamber (Biocare Medical, Pacheco, CA) at a temperature of 95 °C for 20 min. Slides were cooled for 20 min at room temperature and transferred to TRIS buffer with Tween 20 detergent (TBST). The rest of the staining was carried out at room temperature using a BioCare Intellipath stainer (Biocare Medical, Pacheco, CA).

Slides were incubated with 3% hydrogen peroxide in water for 5 min. Slides were rinsed with TBST and incubated in 2.5% normal goat serum for 20 min. Excess reagent was blown off. CD68 (Invitrogen, PA5-78996) was applied at a dilution of 1:500 (1 μ g/mL) for 30 min or CD206 (Proteintech 18704-1-AP) was applied at a dilution of 1:2000 (1 μ g/mL) for 30 min. The negative control slide was stained with Rabbit IgG (Vector Laboratories, I-1000) at a concentration of 1:5000 (1 μ g/mL) for 30 min. A normal mouse tissue array was used as a control. Slides were rinsed twice in TBST and a goat antirabbit secondary (Vector Laboratories, MP-7451) was applied for 30 min. Slides were rinsed twice in TBST, and Vector ImmPACT DAB (Vector Laboratories, SK-4105) was applied for 5 min. Slides were rinsed in water and transferred to a Leica Autostainer XL for hematoxylin counterstain, dehydration, and coverslipping.

All slides were imaged using a Nikon 90i upright microscope equipped with DS-Ri1 camera (Tokyo, Japan) at 4× or 10× magnification and analyzed using ImageJ. Histology and immunochemistry were evaluated and graded by a pathologist in a single-blind review.

Statistical Analysis. All values are reported as average \pm standard deviation. Statistical analysis was performed using one-way analysis of variance (ANOVA) with Bonferroni correction using OriginPro 2018 software (Northampton, MA). A *p*-value lower than 0.05, 0.01, and 0.005 was denoted as *, **, and ***, respectively.

ASSOCIATED CONTENT

Supporting Information

The Supporting Information is available free of charge at https://pubs.acs.org/doi/10.1021/acsami.0c04729.

Figures S1-S15, Tables S1-S3 (PDF)

AUTHOR INFORMATION

Corresponding Author

Hyowon Lee — Weldon School of Biomedical Engineering, Birck Nanotechnology Center, Center for Implantable Devices, Purdue University, West Lafayette, Indiana 47907, United States; orcid.org/0000-0001-7628-1441; Email: hwlee@purdue.edu

Authors

Jian Xu — Weldon School of Biomedical Engineering, Birck Nanotechnology Center, Center for Implantable Devices, Purdue University, West Lafayette, Indiana 47907, United States; orcid.org/0000-0003-4964-6112

Haesoo Moon — Weldon School of Biomedical Engineering, Birck Nanotechnology Center, Center for Implantable Devices, Purdue University, West Lafayette, Indiana 47907, United States; oorcid.org/0000-0001-5190-6441

Jinjia Xu — Weldon School of Biomedical Engineering, Birck Nanotechnology Center, Center for Implantable Devices, Purdue University, West Lafayette, Indiana 47907, United States; orcid.org/0000-0002-5828-8460

Jongcheon Lim — Weldon School of Biomedical Engineering, Birck Nanotechnology Center, Center for Implantable Devices, Purdue University, West Lafayette, Indiana 47907, United States; © orcid.org/0000-0003-2319-0727

Thomas Fischer — School of Engineering Technology, Birck Nanotechnology Center, Purdue University, West Lafayette, Indiana 47907, United States; orcid.org/0000-0002-7784-5234

Helen A. McNally — School of Engineering Technology, Birck Nanotechnology Center, Purdue University, West Lafayette, Indiana 47907, United States; orcid.org/0000-0002-9786-

Herman O. Sintim — Department of Chemistry, Center for Drug Discovery, Purdue Institute of Inflammation, Immunology and Infectious Disease, Purdue University, West Lafayette, Indiana 47907, United States; orcid.org/0000-0002-2280-9359

Complete contact information is available at: https://pubs.acs.org/10.1021/acsami.0c04729

Author Contributions

H.L, H.A.M., and H.O.S. conceived the experiments and supervised the project. J.X. conducted the experiments with the help of H.M. (antibacterial evaluation) and T.F. (AFM). All authors participated in the analysis of the results. The animal study was conducted by J.X., H.M., and J.L. Manuscript was written by J.X. and H.L. All authors reviewed and approved the manuscript.

Notes

The authors declare no competing financial interest.

ACKNOWLEDGMENTS

This work was supported in part by the National Science Foundation (United States) under Grants ECCS-1944480 and CNS-1726865 and in part by Eli Lilly and Company. The authors acknowledge the assistance of V. Bernal-Crespo from Purdue University Histology Research Laboratory, a core facility of the NIH-funded Indiana Clinical and Translational Science Institute, and Purdue Imaging Facility. The authors also like to thank J. A. Christian, DVM, Ph.D. for tissue grading and input in histology reading.

REFERENCES

- (1) Arciola, C. R.; Campoccia, D.; Montanaro, L. Implant Infections: Adhesion, Biofilm Formation and Immune Evasion. *Nat. Rev. Microbiol.* **2018**, *16* (7), 397–409.
- (2) Campoccia, D.; Montanaro, L.; Arciola, C. R. A Review of the Biomaterials Technologies for Infection-Resistant Surfaces. *Biomaterials* **2013**, *34* (34), 8533–8554.
- (3) Rojo, L.; Barcenilla, J. M.; Vázquez, B.; González, R.; San Román, J. Intrinsically Antibacterial Materials Based on Polymeric Derivatives of Eugenol for Biomedical Applications. *Biomacromolecules* **2008**, *9* (9), 2530–2535.
- (4) Foster, H. A.; Ditta, I. B.; Varghese, S.; Steele, A. Photocatalytic Disinfection Using Titanium Dioxide: Spectrum and Mechanism of Antimicrobial Activity. *Appl. Microbiol. Biotechnol.* **2011**, 90 (6), 1847–1868.
- (5) Campoccia, D.; Montanaro, L.; Speziale, P.; Arciola, C. R. Antibiotic-Loaded Biomaterials and the Risks for the Spread of Antibiotic Resistance Following Their Prophylactic and Therapeutic Clinical Use. *Biomaterials* **2010**, *31* (25), 6363–6377.
- (6) Yang, Q.; Park, H.; Nguyen, T. N. H.; Rhoads, J. F.; Lee, A.; Bentley, R. T.; Judy, J. W.; Lee, H. Anti-Biofouling Implantable Catheter Using Thin-Film Magnetic Microactuators. *Sens. Actuators, B* **2018**, 273 (March), 1694–1704.
- (7) Hajipour, M. J.; Fromm, K. M.; Akbar Ashkarran, A.; Jimenez de Aberasturi, D.; de Larramendi, I. R.; Rojo, T.; Serpooshan, V.; Parak, W. J.; Mahmoudi, M. Antibacterial Properties of Nanoparticles. *Trends Biotechnol.* **2012**, *30* (10), 499–511.
- (8) Tripathy, A.; Sen, P.; Su, B.; Briscoe, W. H. Natural and Bioinspired Nanostructured Bactericidal Surfaces. *Adv. Colloid Interface Sci.* **2017**, 248, 85–104.
- (9) Modaresifar, K.; Azizian, S.; Ganjian, M.; Fratila-Apachitei, L. E.; Zadpoor, A. A. Bactericidal Effects of Nanopatterns: A Systematic Review. *Acta Biomater.* **2019**, *83*, 29–36.
- (10) Lin, N.; Berton, P.; Moraes, C.; Rogers, R. D.; Tufenkji, N. Nanodarts, Nanoblades, and Nanospikes: Mechano-Bactericidal Nanostructures and Where to Find Them. *Adv. Colloid Interface Sci.* **2018**, 252, 55–68.
- (11) Jaggessar, A.; Shahali, H.; Mathew, A.; Yarlagadda, P. K. D. V. Bio-Mimicking Nano and Micro-Structured Surface Fabrication for Antibacterial Properties in Medical Implants. *J. Nanobiotechnol.* **2017**, *15* (1), 64.
- (12) Xu, J.; Xu, J.; Moon, H.; Sintim, H. O.; Lee, H. Zwitterionic Porous Conjugated Polymers as a Versatile Platform for Antibiofouling Implantable Bioelectronics. *ACS Appl. Polym. Mater.* **2020**, 2 (2), 528–536.
- (13) Hasan, J.; Webb, H. K.; Truong, V. K.; Pogodin, S.; Baulin, V. A.; Watson, G. S.; Watson, J. A.; Crawford, R. J.; Ivanova, E. P. Selective Bactericidal Activity of Nanopatterned Superhydrophobic Cicada Psaltoda Claripennis Wing Surfaces. *Appl. Microbiol. Biotechnol.* 2013, 97 (20), 9257–9262.
- (14) Bandara, C. D.; Singh, S.; Afara, I. O.; Wolff, A.; Tesfamichael, T.; Ostrikov, K.; Oloyede, A. Bactericidal Effects of Natural Nanotopography of Dragonfly Wing on Escherichia Coli. ACS Appl. Mater. Interfaces 2017, 9 (8), 6746–6760.
- (15) Watson, G. S.; Green, D. W.; Schwarzkopf, L.; Li, X.; Cribb, B. W.; Myhra, S.; Watson, J. A. A Gecko Skin Micro/Nano Structure A Low Adhesion, Superhydrophobic, Anti-Wetting, Self-Cleaning, Biocompatible, Antibacterial Surface. *Acta Biomater.* **2015**, *21*, 109—122
- (16) Ivanova, E. P.; Hasan, J.; Webb, H. K.; Truong, V. K.; Watson, G. S.; Watson, J. A.; Baulin, V. A.; Pogodin, S.; Wang, J. Y.; Tobin, M. J.; Löbbe, C.; Crawford, R. J. Natural Bactericidal Surfaces: Mechanical Rupture of Pseudomonas Aeruginosa Cells by Cicada Wings. *Small* **2012**, *8* (16), 2489–2494.
- (17) Pogodin, S.; Hasan, J.; Baulin, V. A.; Webb, H. K.; Truong, V. K.; Phong Nguyen, T. H.; Boshkovikj, V.; Fluke, C. J.; Watson, G. S.; Watson, J. A.; Crawford, R. J.; Ivanova, E. P. Biophysical Model of Bacterial Cell Interactions with Nanopatterned Cicada Wing Surfaces. *Biophys. J.* **2013**, *104* (4), 835–840.

- (18) Ivanova, E. P.; Hasan, J.; Webb, H. K.; Gervinskas, G.; Juodkazis, S.; Truong, V. K.; Wu, A. H. F.; Lamb, R. N.; Baulin, V. A.; Watson, G. S.; Watson, J. A.; Mainwaring, D. E.; Crawford, R. J. Bactericidal Activity of Black Silicon. *Nat. Commun.* **2013**, *4* (1), 2838
- (19) Hizal, F.; Zhuk, I.; Sukhishvili, S.; Busscher, H. J.; van der Mei, H. C.; Choi, C.-H. Impact of 3D Hierarchical Nanostructures on the Antibacterial Efficacy of a Bacteria-Triggered Self-Defensive Antibiotic Coating. ACS Appl. Mater. Interfaces 2015, 7 (36), 20304–20313.
- (20) Wu, S.; Zuber, F.; Brugger, J.; Maniura-Weber, K.; Ren, Q. Antibacterial Au Nanostructured Surfaces. *Nanoscale* **2016**, 8 (5), 2620–2625.
- (21) Kim, S.; Jung, U. T.; Kim, S.-K.; Lee, J.-H.; Choi, H. S.; Kim, C.-S.; Jeong, M. Y. Nanostructured Multifunctional Surface with Antireflective and Antimicrobial Characteristics. *ACS Appl. Mater. Interfaces* **2015**, *7* (1), 326–331.
- (22) Zhang, G.; Zhang, J.; Xie, G.; Liu, Z.; Shao, H. Cicada Wings: A Stamp from Nature for Nanoimprint Lithography. *Small* **2006**, 2 (12), 1440–1443.
- (23) Diu, T.; Faruqui, N.; Sjöström, T.; Lamarre, B.; Jenkinson, H. F.; Su, B.; Ryadnov, M. G. Cicada-Inspired Cell-Instructive Nanopatterned Arrays. *Sci. Rep.* **2015**, *4* (1), 7122.
- (24) Gillett, A.; Waugh, D.; Lawrence, J.; Swainson, M.; Dixon, R. Laser Surface Modification for the Prevention of Biofouling by Infection Causing Escherichia Coli. *J. Laser Appl.* **2016**, 28 (2), No. 022503.
- (25) Hu, H.; Siu, V. S.; Gifford, S. M.; Kim, S.; Lu, M.; Meyer, P.; Stolovitzky, G. A. Bio-Inspired Silicon Nanospikes Fabricated by Metal-Assisted Chemical Etching for Antibacterial Surfaces. *Appl. Phys. Lett.* **2017**, *111* (25), 253701.
- (26) Chen, J.-K.; Qui, J.-Q.; Fan, S.-K.; Kuo, S.-W.; Ko, F.-H.; Chu, C.-W.; Chang, F.-C. Using Colloid Lithography to Fabricate Silicon Nanopillar Arrays on Silicon Substrates. *J. Colloid Interface Sci.* **2012**, 367 (1), 40–48.
- (27) Ding, J.; Du, K.; Wathuthanthri, I.; Choi, C.-H.; Fisher, F. T.; Yang, E.-H. Transfer Patterning of Large-Area Graphene Nanomesh via Holographic Lithography and Plasma Etching. J. Vac. Sci. Technol., B: Nanotechnol. Microelectron.: Mater., Process., Meas., Phenom. 2014, 32 (6), No. 06FF01.
- (28) Hong, S.-H.; Hwang, J.; Lee, H. Replication of Cicada Wing's Nano-Patterns by Hot Embossing and UV Nanoimprinting. *Nanotechnology* **2009**, *20* (38), 385303.
- (29) Phan, L.; Yoon, S.; Moon, M.-W. Plasma-Based Nanostructuring of Polymers: A Review. *Polymers (Basel, Switz.)* **2017**, 9 (12), 417.
- (30) Dickson, M. N.; Tsao, J.; Liang, E. I.; Navarro, N. I.; Patel, Y. R.; Yee, A. F. Conformal Reversal Imprint Lithography for Polymer Nanostructuring over Large Curved Geometries. J. Vac. Sci. Technol., B: Nanotechnol. Microelectron.: Mater., Process., Meas., Phenom. 2017, 35 (2), No. 021602.
- (31) Flemming, R. G.; Murphy, C. J.; Abrams, G. A.; Goodman, S. L.; Nealey, P. F. Effects of Synthetic Micro- and Nano-Structured Surfaces on Cell Behavior. *Biomaterials* **1999**, *20* (6), 573–588.
- (32) Ainslie, K. M.; Thakar, R. G.; Bernards, D. A.; Desai, T. A. Inflammatory Response to Implanted Nanostructured Materials. In *Biological Interactions on Materials Surfaces*; Puleo, D. A., Bizios, R., Eds.; Springer US: New York, 2009; pp 355–371.
- (33) Nuhn, H.; Blanco, C. E.; Desai, T. A. Nanoengineered Stent Surface to Reduce In-Stent Restenosis in Vivo. ACS Appl. Mater. Interfaces 2017, 9 (23), 19677–19686.
- (34) Serrano, C.; García-Fernández, L.; Fernández-Blázquez, J. P.; Barbeck, M.; Ghanaati, S.; Unger, R.; Kirkpatrick, J.; Arzt, E.; Funk, L.; Turón, P.; del Campo, A. Nanostructured Medical Sutures with Antibacterial Properties. *Biomaterials* **2015**, *52* (1), 291–300.
- (35) Du, K.; Jiang, Y.; Huang, P.-S.; Ding, J.; Gao, T.; Choi, C.-H. Self-Formation of Polymer Nanostructures in Plasma Etching: Mechanisms and Applications. *J. Micromech. Microeng.* **2018**, 28 (1), No. 014006.

- (36) Abourayana, H. M.; Dowling, D. P. Plasma Processing for Tailoring the Surface Properties of Polymers. In *Surface Energy*; Aliofkhazraei, M., Ed.; InTech, 2015.
- (37) Ko, T.-J.; Oh, K. H.; Moon, M.-W. Plasma-Induced Hetero-Nanostructures on a Polymer with Selective Metal Co-Deposition. *Adv. Mater. Interfaces* **2015**, 2 (1), 1400431.
- (38) Morber, J. R.; Wang, X.; Liu, J.; Snyder, R. L.; Wang, Z. L. Wafer-Level Patterned and Aligned Polymer Nanowire/Micro- and Nanotube Arrays on Any Substrate. *Adv. Mater.* **2009**, 21 (20), 2072–2076.
- (39) Heinemann, L.; Krinelke, L. Insulin Infusion Set: The Achilles Heel of Continuous Subcutaneous Insulin Infusion. *J. Diabetes Sci. Technol.* **2012**, *6* (4), 954–964.
- (40) Soto-Gutiérrez, A.; Kobayashi, N.; Rivas-Carrillo, J. D.; Navarro-Álvarez, N.; Zhao, D.; Okitsu, T.; Noguchi, H.; Basma, H.; Tabata, Y.; Chen, Y.; Tanaka, K.; Narushima, M.; Miki, A.; Ueda, T.; Jun, H.-S.; Yoon, J.-W.; Lebkowski, J.; Tanaka, N.; Fox, I. J. Reversal of Mouse Hepatic Failure Using an Implanted Liver-Assist Device Containing ES Cell—Derived Hepatocytes. *Nat. Biotechnol.* **2006**, 24 (11), 1412—1419.
- (41) Mangano, F.; Zecca, P.; Pozzi-Taubert, S.; Macchi, A.; Ricci, M.; Luongo, G.; Mangano, C. Maxillary Sinus Augmentation Using Computer-Aided Design/Computer-Aided Manufacturing (CAD/CAM) Technology. *Int. J. Med. Robot. Comput. Assist. Surg.* **2013**, 9 (3), 331–338.
- (42) Benic, G. I.; Hämmerle, C. H. F. Horizontal Bone Augmentation by Means of Guided Bone Regeneration. *Periodontol.* 2000 **2014**, 66 (1), 13–40.
- (43) Economou, D. J. Modeling and Simulation of Plasma Etching Reactors for Microelectronics. *Thin Solid Films* **2000**, *365* (2), 348–367.
- (44) Dean, J. A. Lange's Handbook of Chemistry, 15th ed.; McGraw-Hill: New York, 1999.
- (45) Kushner, M. J. A Kinetic Study of the Plasma-Etching Process. II. Probe Measurements of Electron Properties in an Rf Plasma-Etching Reactor. *J. Appl. Phys.* **1982**, 53 (4), 2939–2946.
- (46) Boswell, R. W.; Morey, I. J. Self-consistent Simulation of a Parallel-plate Rf Discharge. *Appl. Phys. Lett.* **1988**, 52 (1), 21–23.
- (47) Kushner, M. J. Monte-Carlo Simulation of Electron Properties in Rf Parallel Plate Capacitively Coupled Discharges. *J. Appl. Phys.* **1983**, *54* (9), 4958–4965.
- (48) Gogolides, E.; Constantoudis, V.; Kokkoris, G.; Kontziampasis, D.; Tsougeni, K.; Boulousis, G.; Vlachopoulou, M.; Tserepi, A. Controlling Roughness: From Etching to Nanotexturing and Plasma-Directed Organization on Organic and Inorganic Materials. *J. Phys. D: Appl. Phys.* **2011**, *44* (17), 174021.
- (49) Ryu, J.; Kim, K.; Park, J.; Hwang, B. G.; Ko, Y.; Kim, H.; Han, J.; Seo, E.; Park, Y.; Lee, S. J. Nearly Perfect Durable Superhydrophobic Surfaces Fabricated by a Simple One-Step Plasma Treatment. Sci. Rep. 2017, 7 (1), 1981.
- (50) Wenzel, R. N. RESISTANCE OF SOLID SURFACES TO WETTING BY WATER. Ind. Eng. Chem. 1936, 28 (8), 988–994.
- (51) Cassie, A. B. D.; Baxter, S. Wettability of Porous Surfaces. *Trans. Faraday Soc.* **1944**, *40*, 546.
- (52) Agarwal, N.; Ponoth, S.; Plawsky, J.; Persans, P. D. Roughness Evolution in Polyimide Films during Plasma Etching. *Appl. Phys. Lett.* **2001**, 78 (16), 2294–2296.
- (53) Memos, G.; Lidorikis, E.; Kokkoris, G. Roughness Evolution and Charging in Plasma-Based Surface Engineering of Polymeric Substrates: The Effects of Ion Reflection and Secondary Electron Emission. *Micromachines* **2018**, *9* (8), 415.
- (54) Epstein, A. K.; Hochbaum, A. I.; Kim, P.; Aizenberg, J. Control of Bacterial Biofilm Growth on Surfaces by Nanostructural Mechanics and Geometry. *Nanotechnology* **2011**, 22 (49), 494007.
- (55) Li, X. Bactericidal Mechanism of Nanopatterned Surfaces. *Phys. Chem. Chem. Phys.* **2016**, *18* (2), 1311–1316.
- (56) Li, X.; Chen, T. Enhancement and Suppression Effects of a Nanopatterned Surface on Bacterial Adhesion. *Phys. Rev. E: Stat.*

- Phys., Plasmas, Fluids, Relat. Interdiscip. Top. 2016, 93 (5), No. 052419.
- (57) Linklater, D. P.; De Volder, M.; Baulin, V. A.; Werner, M.; Jessl, S.; Golozar, M.; Maggini, L.; Rubanov, S.; Hanssen, E.; Juodkazis, S.; Ivanova, E. P. High Aspect Ratio Nanostructures Kill Bacteria via Storage and Release of Mechanical Energy. *ACS Nano* **2018**, *12* (7), 6657–6667.
- (58) Ohkubo, Y.; Ishihara, K.; Shibahara, M.; Nagatani, A.; Honda, K.; Endo, K.; Yamamura, K. Drastic Improvement in Adhesion Property of Polytetrafluoroethylene (PTFE) via Heat-Assisted Plasma Treatment Using a Heater. Sci. Rep. 2017, 7 (1), 9476.
- (59) Youxian, D.; Griesser, H. J.; Mau, A. W. H.; Schmidt, R.; Liesegang, J. Surface Modification of Poly(Tetrafluoroethylene) by Gas Plasma Treatment. *Polymer* 1991, 32 (6), 1126–1130.
- (60) Ryan, M. E.; Badyal, J. P. S. Surface Texturing of PTFE Film Using Nonequilibrium Plasmas. *Macromolecules* **1995**, 28 (5), 1377–1382.
- (61) Xu, H.; Mandal, M. Epidermis Segmentation in Skin Histopathological Images Based on Thickness Measurement and K-Means Algorithm. *EURASIP J. Image Video Process.* **2015**, 2015 (1), 18
- (62) Ibrahim, M.; Bond, J.; Medina, M.A.; Chen, L.; Quiles, C.; Kokosis, G.; Bashirov, L.; Klitzman, B.; Levinson, H. Characterization of the Foreign Body Response to Common Surgical Biomaterials in a Murine Model. *Eur. J. Plast. Surg.* **2017**, *40* (5), 383–392.
- (63) Boddupalli, A.; Zhu, L.; Bratlie, K. M. Methods for Implant Acceptance and Wound Healing: Material Selection and Implant Location Modulate Macrophage and Fibroblast Phenotypes. *Adv. Healthcare Mater.* **2016**, 5 (20), 2575–2594.
- (64) Zhang, L.; Cao, Z.; Bai, T.; Carr, L.; Ella-Menye, J.-R.; Irvin, C.; Ratner, B. D.; Jiang, S. Zwitterionic Hydrogels Implanted in Mice Resist the Foreign-Body Reaction. *Nat. Biotechnol.* **2013**, 31 (6), 553–556.
- (65) Chandorkar, Y. K. R.; Basu, B. The Foreign Body Response Demystified. ACS Biomater. Sci. Eng. 2019, 5 (1), 19–44.
- (66) Bryers, J. D.; Giachelli, C. M.; Ratner, B. D. Engineering Biomaterials to Integrate and Heal: The Biocompatibility Paradigm Shifts. *Biotechnol. Bioeng.* **2012**, *109* (8), 1898–1911.
- (67) Liu, T.; Kim, C.-J. Turning a Surface Superrepellent Even to Completely Wetting Liquids. *Science (Washington, DC, U. S.)* **2014**, 346 (6213), 1096–1100.
- (68) Jiang, Y.; Xu, J.; Lee, J.; Du, K.; Yang, E.-H.; Moon, M.-W.; Choi, C.-H. Nanotexturing of Conjugated Polymers via One-Step Maskless Oxygen Plasma Etching for Enhanced Tunable Wettability. *Langmuir* **2017**, 33 (27), 6885–6894.
- (69) Sainiemi, L.; Jokinen, V.; Shah, A.; Shpak, M.; Aura, S.; Suvanto, P.; Franssila, S. Non-Reflecting Silicon and Polymer Surfaces by Plasma Etching and Replication. *Adv. Mater.* **2011**, 23 (1), 122–126.
- (70) Fan, X.; Chen, J.; Yang, J.; Bai, P.; Li, Z.; Wang, Z. L. Ultrathin, Rollable, Paper-Based Triboelectric Nanogenerator for Acoustic Energy Harvesting and Self-Powered Sound Recording. *ACS Nano* **2015**, 9 (4), 4236–4243.
- (71) Carson, F. L.; Cappellano, C. H. Histotechnology: A Self Instructional Text; ASCP: Chicago, 2015.